

Accepted for publication in *Journal of Geophysical Research Atmospheres*.

Copyright 2015 American Geophysical Union. Further reproduction or electronic distribution is not permitted.

¹ **Optical modeling of volcanic ash particles using** ² **ellipsoids**

Sini Merikallio¹, Olga Muñoz², Anu-Maija Sundström³, Timo H. Virtanen¹,

Matti Horttanainen¹, Gerrit de Leeuw^{1,3}, Timo Nousiainen¹

Corresponding author: S. Merikallio, Finnish Meteorological Institute, Erik Palménin aukio 1,
FI-00560 Helsinki, Finland. (sini.merikallio@fmi.fi)

¹Finnish Meteorological Institute,
Helsinki, Finland.

²Instituto de Astrofísica de Andalucía,
CSIC, Spain.

³Department of Physics, University of
Helsinki, Helsinki, Finland.

3 **Abstract.** The single-scattering properties of volcanic ash particles are
4 modeled here by using ellipsoidal shapes. Ellipsoids are expected to improve
5 accuracy of remote sensing retrievals, which are currently often based on over-
6 simplified assumptions of spherical ash particles. Measurements of the single-
7 scattering optical properties of ash particles from several volcanoes across
8 the globe, including previously unpublished measurements from the Eyjaf-
9 jallajökull and Puyehue volcanoes, are used to assess the performance of the
10 ellipsoidal particle models. These comparisons between the measurements
11 and the ellipsoidal particle model include consideration of the whole scat-
12 tering matrix, as well as sensitivity studies on the point of view of the AATSR
13 satellite instrument. AATSR, which flew on the ENVISAT satellite, offers
14 two viewing directions but no information on polarization, so usually only
15 the phase function is relevant for interpreting its measurements.

16 As expected, ensembles of ellipsoids are able to reproduce the observed scat-
17 tering matrix more faithfully than spheres. Performance of ellipsoid ensem-
18 bles depends on the distribution of particle shapes, which we tried to opti-
19 mize. No single specific shape distribution could be found that would per-
20 form superiorly in all situations, but all of the best-fit ellipsoidal distribu-
21 tions, as well as the additionally tested equiprobable distribution, improved
22 greatly over the performance of spheres. We conclude that an equiprobable
23 shape distribution of ellipsoidal particles is a relatively good, yet enticingly
24 simple, approach for modeling volcanic ash single-scattering optical prop-
25 erties.

1. Introduction

26 Volcanic eruptions, in particular the explosive types, may generate vast amounts of
27 volcanic ash, which is then dispersed in the atmosphere. This ash can be transported
28 over large distances, depending on the plume height, meteorological conditions and ash
29 particle size. By absorbing, emitting and scattering electromagnetic radiation, processes
30 all described by so-called optical properties, these particles may induce considerable en-
31 vironmental impacts [*Bertrand et al.*, 1999; *Mather et al.*, 2013; *Bignami et al.*, 2013],
32 potentially even blurring the effects of anthropogenic climate change for a while [*Hyde*
33 *and Crowley*, 2000; *Bertrand et al.*, 2002]. In addition to radiative effects, volcanic prod-
34 ucts can also change atmospheric chemistry considerably [*McGee et al.*, 1994] and induce
35 health hazards, especially respiratory problems [*Baxter et al.*, 1982; *Horwell and Baxter*,
36 2006; *Gudmundsson*, 2011]. These health effects depend on particle properties; namely
37 size, composition and surface characteristics [*Horwell and Baxter*, 2006], all of which can
38 vary between sources and even as a function of the ash plume age due to chemical and phys-
39 ical processes taking place within the newly erupted matter [*Mather et al.*, 2013]. These
40 same traits also affect the way ash particles scatter and absorb light, namely refractive
41 index of the scattering material, scattering and absorption cross-sections, and scattering
42 phase function. Also, we are not able to forecast volcanic eruptions well [*Sparks*, 2003]
43 and while in the atmosphere, ash particles may interfere with aviation activities causing
44 considerable economic losses [*Casadevall*, 1994; *Guffanti et al.*, 2010; *Prata et al.*, 2014].
45 For these reasons the remote detection and global monitoring of ash clouds is of great
46 interest.

47 Volcanic ash particles are irregularly shaped and can be substantially porous [*Heiken,*
48 1974; *Riley et al.*, 2003]. Modeling optical properties of such particles accurately can be
49 extremely challenging, while being crucially important for reliable remote sensing observa-
50 tions of atmospheric ash. Inadequate optical models may lead, for example, to ash plumes
51 misidentified as other types of particles by the retrieval algorithm, as happened with
52 the MISR (Multi-angle Imaging SpectroRadiometer) satellite instrument during Eyjafjal-
53 lajökull eruption [*Kahn and Limbacher*, 2012]. Also, present satellite retrieval algorithms
54 may be unable to identify large ash particles [*Stevenson et al.*, 2015; *Kylling et al.*, 2014].
55 As of yet, optical modeling based on morphologically faithful model particles cannot cover
56 the whole range of optically important ash particles present in the atmosphere [*Kahnert*
57 *et al.*, 2014]. It is thus highly desirable to establish whether simpler model particles could
58 be used to mimic the volcanic ash optical properties adequately, which is why we study
59 here whether simple yet flexible ellipsoidal model particles could be used as a proxy for
60 ash in remote sensing retrievals. This is done by comparing model simulations based on
61 ellipsoids with laboratory-measured scattering matrices for real volcanic ash samples. We
62 also investigate the performance of the ellipsoid model for use with the AATSR (Advanced
63 Along Track Scanning Radiometer) retrievals, taking into account the specific angle span
64 visible to the instrument, and focusing on the phase function.

65 The shape of an ellipsoid greatly affects the way it scatters light. Scattering by an
66 ensemble of ellipsoids is thus dependent on the relative proportions of different shapes,
67 i.e. the shape distribution of the ensemble. We aim at deriving a generic shape distribution
68 of ellipsoidal model particles that would closely mimic scattering by volcanic ash particles
69 and could thus be used as a first guess in modeling light scattering by ash of any volcano.

70 Because volcanic ash particles are neither ellipsoidal nor homogenous, it is far from
71 obvious that such particles could mimic the optical properties of ash particles realisti-
72 cally. Therefore, we test not only the performance of ellipsoids in mimicking the optical
73 properties of volcanic ash particles, but also analyze the shape distributions that provide
74 the best performance for different laboratory data. The latter is to establish whether a
75 generic shape distribution could be proposed for the optical modeling of ash particles. It
76 is noted that, if the shape distribution can be fixed, then the optical properties predicted
77 by ellipsoids depend only on the refractive index and size parameter, exactly as is the
78 case for Mie spheres, making the application of ellipsoids simpler. The fact that ellipsoids
79 have been previously shown to mimic well the optical properties of mineral dust particles
80 present in the terrestrial and Martian atmosphere [*Bi et al.*, 2009; *Merikallio et al.*, 2013],
81 which are also non-ellipsoidal and inhomogeneous particles, suggest that ellipsoids might
82 nevertheless perform adequately also for mimicking ash optical properties.

83 Figure 1 shows the locations of all volcanoes from which the ash samples studied in
84 this paper were collected. A number of different samples collected from world-wide lo-
85 cations are used to assure that the findings are generic. Eyjafjallajökull and Puyehue
86 ash scattering measurements are presented in this paper, but others have been published
87 before by *Volten et al.* [2001] and *Muñoz et al.* [2004]. The locations are scattered widely
88 over the globe, emphasizing the global relevance of volcanic eruptions. Sampled volca-
89 noes are situated in subduction zones except Eyjafjallajökull, which lies in a rift zone.
90 All of these volcanoes can produce ash clouds as a result of the explosive nature of their
91 eruptions. Partly this is a result of their mineral compositions, particularly the relatively
92 high amount of SiO_2 in magma and partly of interaction with water, as is the case with

93 Eyjafjallajökull [*Gudmundsson et al.*, 2008]. Composition and optical characteristics of
94 the samples can be expected to vary. Thus, if a model is found that works adequately in
95 modeling all of the samples, it can reasonably be expected to perform adequately also on
96 modeling future eruptions, regardless of their location.

2. Laboratory Measurements

97 Measurements are needed as a reference to which the modeling approach, i.e. using
98 ellipsoidal particles to model optical properties of the volcanic ash particles (as described
99 in Section 3), can be compared to assess the validity of this approach. In this section we
100 present and discuss new light scattering measurements (scattering matrices) measurements
101 for Eyjafjallajökull and Puyehue volcanic ash samples. The measurements have been
102 performed at the IAA CODULAB in Granada. The measurements corresponding to the
103 other volcanic ash samples considered in this paper, namely Pinatubo, Lokon, Mount St.
104 Helens, Spurr Ashton and Redoubt volcanoes, were performed at the Amsterdam Light
105 scattering setup [*Hovenier*, 2000] and have previously been published by *Volten et al.*
106 [2001] and *Muñoz et al.* [2004].

2.1. Volcanic Ash Samples

107 The Puyehue ash sample originates from the June 2011 eruption of the Puyehue-Cordón
108 Caulle complex. The sample was collected from the surface deposit at a distance of around
109 150 km from the epicenter of the eruption in the Comallo region. A rhyolitic obsidian
110 composition could be assumed for the Puyehue ash [*Newman et al.*, 2012] with the complex
111 refractive index m of $1.48 + 0.00027i$ [*Pollack et al.*, 1974].

112 The Eyjafjallajökull ash sample was collected from the surface deposit right after the
113 April 2010 eruption at 5 km from the source. Estimates of the real part of the refractive
114 index in the spectral region at which we have performed our light scattering measurements
115 (647.0 nm) range from 1.43 [Newman *et al.*, 2012] to 1.49 for the fine grain mode (diameter
116 0.1 - 0.6 μm), and from 1.52 [Newman *et al.*, 2012] to 1.59 [Schumann *et al.*, 2011] for the
117 coarse mode (diameter of 0.6 - 35 μm). The imaginary part varies from non-absorbing
118 particles [Schumann *et al.*, 2011; Newman *et al.*, 2012] to 0.0012 [Rocha-Lima *et al.*, 2014]
119 for the fine mode and 0.0015 [Newman *et al.*, 2012; Rocha-Lima *et al.*, 2014] to 0.004
120 [Schumann *et al.*, 2011] for the coarse mode. In the modeling part of this work, however,
121 we have decided to use a different refractive index value of $1.55 + 0.001i$ for both Puyehue
122 and Eyjafjallajökull samples because this produced better fits, as explained in Section 3.

123 In Figure 2 we present Scanning Electron Microscope (SEM) images of the samples
124 discussed in this paper, including those of the Eyjafjallajökull and Puyehue ash particles.
125 These particles show the characteristic shapes of volcanic ash particles [Maria and Carey,
126 2002; Riley *et al.*, 2003]. In particular, they contain vesicular (interspersed by cavities)
127 particles and crystals with sharp edges. It should be noted that these SEM pictures are
128 not representative for the particle size distributions of the samples; for that purpose, we
129 refer the reader to the next subsection.

2.2. Size Distribution Measurements

130 The volume distribution of the Eyjafjallajökull and Puyehue samples were measured
131 with a Mastersizer2000 from Malvern instruments; these volume distributions were then
132 converted to number size distributions. The Mastersizer2000 measures the phase function
133 of the sample at a wavelength of 632.8 nm over a certain range of scattering angles

134 with special attention to the forward scattering peak. The measured phase function
135 is used to retrieve the volume distribution by matching the angular patterns to those
136 simulated by the instrument software. In the simulations, either Lorenz-Mie or Fraunhofer
137 theory is applied. Both options make an inherent assumption that the measured particles
138 are spherical. Moreover, unlike the Lorenz-Mie method, the Fraunhofer method is an
139 approximation which is not suitable for particles with sizes similar or smaller to that of
140 the instrument's wavelength. As our volcanic ash samples contain particles with sizes
141 from sub-micron scales, it must be assumed that the Lorenz-Mie option might provide
142 more accurate size distribution measurements in the mentioned size range. In general, as
143 is shown in Table 1, the retrieved effective radii from the Lorenz-Mie theory are larger
144 than those obtained with the Fraunhofer theory. As expected, results of both sizing
145 methods tend to converge as the particles become larger. The retrieved size distributions
146 for Puyehue and Eyjafjallajökull samples are shown in Figure 3.

147 The size distributions of the Pinatubo, Lokon, Mount St. Helens, Redoubt A and Mount
148 Spurr samples were measured in Amsterdam by using a Fritsch laser particle sizer [*Kon-*
149 *ert and Vandenberghe, 1997*] that employs the Fraunhofer diffraction theory for spheres.
150 This instrument measures a projected surface-area distribution, which is then converted
151 to number size distribution. As the Fritsch laser sizer does not have the option to use the
152 exact Lorenz-Mie theory, these samples were measured again, about 10 years later, with
153 the Mastersizer2000 in Granada, Spain. When using the Fraunhofer mode, values for the
154 effective radius, r_{eff} , and effective variance, ν_{eff} (as defined in [*Hansen and Travis, 1974*]),
155 similar to those obtained in Amsterdam were only obtained for the St. Helens sample, for
156 which $r_{\text{eff}} = 4.1 \mu\text{m}$ and $\nu_{\text{eff}} = 9.5$ were measured in Amsterdam and $r_{\text{eff}} = 4.3 \mu\text{m}$ and

157 $\nu_{\text{eff}} = 8.1$ ten years later in Granada. This finding provides confidence in that the size
158 distribution retrieved from the Mount St. Helens sample has not significantly changed in
159 time (due to e.g. atmospheric humidity). Therefore, we also retrieved the size distribu-
160 tion for it again in Granada by using the Lorenz-Mie mode. For the other samples later
161 size distribution retrievals are either lacking or deliver over $0.4 \mu\text{m}$ larger values for the
162 effective radius, sowing doubt on the representativeness of using the newer measurements
163 in connection with the scattering matrices measured in Amsterdam. For these reasons
164 we consider the samples in two groups: one for which we have trustworthy Lorenz-Mie
165 measurements available (Mount St. Helens, Puyehue and Eyjafjallajökull), and the other
166 for which we used the originally measured Fraunhofer size-distribution (Pinatubo, Lokon,
167 Redoubt A and Mount Spurr). The calculated effective radii and variances, estimated
168 refractive indices, and the wavelengths for which the scattering matrices have been mea-
169 sured are summarized in Table 1. Tables for normalized number, projected-surface-area,
170 and volume size distributions for the volcanic ash samples are available in the Amsterdam-
171 Granada Light Scattering Database [*Muñoz et al.*, 2010].

2.3. Scattering Measurements

172 The scattering matrices of the Eyjafjallajökull and Puyehue samples were measured at
173 the IAA COsmic DUst LABoratory (CODULAB) located at the Instituto de Astrofísica de
174 Andalucía, Granada, Spain. Briefly, as a light source we use an Argon-Krypton laser tuned
175 at 647 nm. The laser beam passes through a polarizer and an electro-optic modulator.
176 The modulated light is subsequently scattered by an ensemble of randomly oriented ash
177 particles located in a jet stream produced by an aerosol generator. The scattered light
178 passes through a quarter-wave plate and an analyzer (both optional) and is detected by

179 a photomultiplier tube which moves along a ring. In this way scattering angles from
180 3° to 177° are covered in the measurements. Another photomultiplier tube located at
181 a fixed position is used to detect and correct for fluctuations in the signal. We employ
182 polarization modulation in combination with lock-in detection to obtain the entire four-by-
183 four scattering matrix. Special tests have been performed to ensure that our experiment
184 is performed under the single-scattering regime [Muñoz *et al.*, 2011]. We also check that
185 the measurements fulfill the Cloude coherency matrix test given in [Hovenier *et al.*, 1986]
186 within the experimental errors at all measured scattering angles. For a detailed description
187 of the experimental apparatus, calibration process, and data acquisition we refer to [Muñoz
188 *et al.*, 2010].

189 The measured scattering matrices for the Eyjafjallajökull and Puyehue samples at 647
190 nm are presented in Figure 4. The measured scattering matrix \mathbf{F} is related to the phase
191 matrix \mathbf{P} by $\mathbf{F} = a\mathbf{P}$, where a is some unknown normalization factor. All matrix elements
192 (except F_{11} itself) are normalized to F_{11} , that is, we consider F_{ij}/F_{11} , with $ij = 12, 22,$
193 $33, 34,$ or 44 . Due to the unknown a , values of $F_{11}(\theta)$ are re-normalized so that F_{11}
194 equals unity at the scattering angle $\theta = 30^\circ$, thus making different samples comparable.
195 The measurements are presented together with the average scattering matrix for volcanic
196 ashes obtained from the measured scattering matrices of nine volcanic ash samples from
197 the Mount St. Helens, Redoubt, Mount Spurr, Lokon, and Pinatubo volcanoes [Muñoz
198 *et al.*, 2004]. Measurements of those nine samples were performed at 632.8 nm. The
199 domains occupied by the measurements used to obtain the average are shown as a gray
200 area in the background of Figure 4. As shown, the measured scattering matrix for the
201 Eyjafjallajökull and Puyehue samples agree well with both the overall features present

202 in the average scattering matrix and their magnitude. It is interesting to note that the
203 F_{34}/F_{11} ratio in the forward scattering lobe for the Puyehue sample has values larger than
204 any other volcano sample measured.

205 For the use of the results in radiative transfer calculations the full scattering matrix,
206 from 0° to 180° , is needed. Hence the measured scattering matrix data needs to be
207 extended to include the extreme forward and back-scattering angles. This is achieved by
208 constructing so-called synthetic scattering matrices from the measurements in the way
209 described in *Muñoz et al.* [2007] but including conditions at exact forward and backward
210 directions as suggested by *Hovenier and Guirado* [2014].

211 Tables with the experimental data and the corresponding extrapolated matrices
212 for all samples are available at the Amsterdam-Granada light scattering database
213 <http://www.iaa.es/scattering/> [*Muñoz et al.*, 2012].

3. Modeling Approach

214 To investigate whether ellipsoidal model particles can be used in scattering computations
215 to mimic the optical properties of volcanic ash particles, model simulations based on
216 ellipsoids are compared with laboratory-measured scattering matrices for real volcanic ash
217 samples. Different assumptions about the porosity are tested in the simulations and size
218 distributions of volcanic samples derived using Lorenz-Mie and Fraunhofer-based theories
219 are both considered. Apart from the new measurements (performed at a wavelength of
220 647 nm) and the volcanic ashes average (632.8 nm), measurements at 441.6 nm are also
221 considered for those samples for which the measurements in the blue are available, namely
222 Lokon and Pinatubo.

223 The scattering matrices and scattering cross sections of the ellipsoids are retrieved from
 224 the database of *Meng et al.* [2010], where they are tabulated for various refractive indices
 225 (real part $\text{Re}(m)$ ranging from 1.1 to 2.1, and imaginary part $\text{Im}(m)$ from 0.0005 up to 0.5)
 226 and for axis ratios (a_x/a_z and a_y/a_z ranging from unity up to 3.3). The optical properties
 227 for each ellipsoidal shape are obtained from this database using volume-equivalent sizes
 228 and then integrated over the measured size distributions (Sec. 2.2) of the volcanic ash
 229 samples, after which a Monte Carlo fitting procedure is applied to derive an optimal
 230 ellipsoidal shape distribution that minimizes the difference between the modeled and
 231 measured scattering matrices.

232 For computational reasons we need to constrain the fitting of shape distribution into a
 233 manageable amount of shapes. We have thus chosen a carefully selected subset of shapes
 234 present in the database. Namely, ellipsoids with shapes close to a sphere (values of axis
 235 ratios a_x/a_z and a_y/a_z close to unity), but not the sphere itself ($a_x = a_y = a_z$), have been
 236 left out of the analysis. This choice is based on previous studies which showed that best-
 237 fit shape distributions for mineral dusts consists mostly of the noticeably non-spherical
 238 shapes [*Merikallio et al.*, 2011, 2013].

239 For validation, the model results were compared to the experimental data (Sec. 2) and
 240 the best-fit was selected based on the cost function E defined as:

$$241 \quad E = \sum_{\theta} \frac{\varrho_{\theta} [S(\theta) - O(\theta)]^2}{\pi \sigma_{\theta}^2}, \quad (1)$$

242 where $S(\theta)$ is the simulated quantity and $O(\theta)$ the corresponding observed quantity, σ_{θ}
 243 denotes the measured scattering angle dependent standard deviation and ϱ_{θ} is the width
 244 of the angular bin. $S(\theta) = P_{xy}(\theta)/P_{11}(\theta)$ and $O(\theta) = F_{xy}(\theta)/F_{11}(\theta)$, where the xy sub-
 245 script denotes the corresponding scattering matrix element, being 12, 22, 33, 34 or 44.

246 Measurements of the scattering matrix elements include an unknown normalization con-
 247 stant, which can be omitted when only quantities related to the phase function F_{11} are
 248 examined. As the phase function itself is not a relative quantity, its cost function is
 249 defined slightly differently to make it a relative quantity and thus comparable with the
 250 other scattering matrix elements: $E_{11} = \sum_{\theta} \varrho_{\theta} / \pi (P_{11}/F_{11} - 1)^2 / \sigma_{\theta}^2$. Note also that this
 251 definition automatically assures that the forward angles with much higher absolute values
 252 do not dominate the cost function. Each shape-distribution fitting was carried out using
 253 multiple initial conditions to better assure that the global best fit is found.

254 We also made an effort to account for the porosity by applying the effective medium
 255 approximation to compute the corresponding effective refractive indices for different de-
 256 grees of porosity, namely $m = 1.4 + 0.000758i$ corresponding to a porosity of 31.6%,
 257 $1.5 + 0.000921i$ corresponding to 10.9%, and $1.55 + 0.001i$ corresponding to 0% (solid mat-
 258 ter) [*Mishchenko et al.*, 2000]. For simplicity, the same values were used for all samples,
 259 although in reality they are estimated to have differing refractive indices (see Table 1).
 260 This simplification is justifiable by the fact that the estimation of the refractive index
 261 has a high uncertainty and is often based on simplifying assumptions of the composition
 262 equaling some other well-known substance which may or may not accurately describe the
 263 bulk matter composition of the scattering target particle [*Mackie et al.*, 2014]. All the
 264 samples were fitted using all assumptions about porosity (different refractive indices). For
 265 all of our samples, the cost function was best minimized when using the assumed refrac-
 266 tive index of the bulk matter, $1.55 + 0.001i$. This implies that either the particles are
 267 not porous or, more likely, their porosity does not manifest itself in scattering in such
 268 a way that it can be accounted for by using an effective refractive index. The latter is

269 also consistent with findings by [Nousiainen *et al.*, 2011]. However, it was also noted that
270 for some of the samples, in particularly for Eyjafjallajökull, the fits would have slightly
271 improved by using an even smaller imaginary part of the refractive index. This does not
272 necessarily mean that the imaginary parts really are smaller, however; a recent study by
273 *Kemppinen et al.* [2015] shows that ellipsoids may better mimic scattering by irregularly
274 shaped target particles when a wrong refractive index is used. Thus, for simplicity, we
275 decided to use the bulk matter refractive index for all samples throughout this study.

4. Results

276 In our calculations we used the size distributions retrieved from both Fraunhofer and
277 Lorenz-Mie theories. As the size distributions calculated with the Lorenz-Mie theory
278 turned out to provide the best fits, we chose to use those for modeling all the scattering
279 matrices for which we had them reliably available for, namely Eyjafjallajökull, Puyehue
280 and St. Helens. As explained in Section 2.2, the Lorenz-Mie theory based size distribution
281 is not available for Pinatubo, Lokon, Redoubt, and Mt. Spurr ash samples. In those cases,
282 we used the original Fraunhofer size distribution.

4.1. Overall Performance of Ellipsoids

283 In Figure 5 the whole-matrix best-fit ellipsoidal model results based on $m = 1.55 + 0.001i$
284 are shown for Eyjafjallajökull, Puyehue, and St. Helens volcanic ash samples, for which
285 we had reliable Lorenz-Mie-based size measurements available. For brevity, only the most
286 commonly used matrix elements (P_{11} , P_{12}/P_{11} and P_{22}/P_{11}) are shown, although the
287 fitting was performed by optimizing the agreement with all six non-zero matrix elements
288 with equal weights. The phase function P_{11} is shown in logarithmic scale and normalized

289 such that the integral over the scattering angle θ is

$$290 \quad \frac{1}{2} \int_0^\pi P_{11}(\theta) \sin(\theta) d\theta = 1. \quad (2)$$

291 The full angle span of the phase function needed to perform this integral has been achieved
292 by extrapolating the measurements with the mean of model ellipsoid phase functions. Note
293 that here, due to the availability of ellipsoid simulations, we have used this slightly different
294 extrapolation method to that of the released measurements in the Granada database (see
295 Sec. 2.3).

296 Similar data for the other four volcanic ash samples with Fraunhofer size distributions
297 are shown in Figure 6. In addition to the measured values, these plots show the results
298 for the best-fit ellipsoids, Lorenz-Mie model (spherical particles), and the equiprobable
299 ellipsoidal distribution, where all shapes are present in equal proportions. Additionally the
300 whole value span covered by different ellipsoidal shapes is shown as the gray shaded area.
301 It is evident that ellipsoids improve greatly on the performance of spheres in reproducing
302 the optical properties of real ash particles. Still, even the best-fit results are far from
303 perfect and lack performance especially for the depolarization element P_{22}/P_{11} . In part,
304 this may be due to ellipsoids not having rough surfaces, which is not taken into account
305 here [*Nousiainen and Muinonen, 2007; Baum et al., 2010*]. It is noted that the fit from
306 P_{22}/P_{11} could be improved by fitting solely that matrix element, at the expense of other
307 matrix elements for which the fits would then become worse. Overall, ellipsoids perform
308 significantly better than spheres, which are strikingly bad especially with P_{12}/P_{11} , for
309 which they even seem to have the wrong sign, and with P_{22}/P_{11} for which their solution
310 is, by definition, exactly one at all scattering angles.

311 The last row of plots in Figure 5 shows the best-fit shape distributions of ellipsoids for
312 Eyjafjallajökull, St. Helens, and Puyehue, respectively, as a function of the model particle
313 shape axis ratios, a_x/a_z and a_y/a_z . In this projection the prolate spheroids ($a_x > a_y =$
314 a_z) fall on the x-axis, and the oblate spheroids ($a_y = a_x > a_z$) are on the diagonal. The
315 particle non-sphericity increases towards the right and up. It can be seen that the best-
316 fit shape distributions differ quite significantly case by case, but nevertheless share some
317 common characteristics: they all seem to have distributions weighted on the prolate side,
318 but curiously include only a few pure prolates (the x-axis). The same trend can be seen
319 in Figure 7a, where the average shape distribution of all seven samples at all wavelengths
320 is shown. It can be seen that the average best-fit distributions, when fitting the whole
321 matrix, consists mostly of pure ellipsoids and slightly deformed spheroids. The pattern
322 is delightfully similar for the shorter and longer wavelengths, when considered separately
323 (Figure 7b; c).

4.2. Validation in the AATSR Instrument Framework

324 Satellites are important in observing volcanic ash clouds, since they can provide a daily
325 view of an extended area of hundreds to thousands of square kilometers, depending on the
326 instrument characteristics. The purpose of this section is to perform an initial assessment
327 of our results in the context of satellite retrievals. For this, we use the AATSR (Advanced
328 Along Track Scanning Radiometer) as an example because this instrument has been used
329 by our group previously, including prior volcanic ash studies by *Virtanen et al.* [2014].

330 AATSR flew onboard ENVISAT (ENVIronmental SATelite, operating 2002-2012). It
331 offers seven wavebands in the visible (VIS), near-infrared (NIR) and thermal infrared
332 (TIR) [*Llewellyn-Jones et al.*, 2001] and is used for remote sensing of aerosol prop-

333 erties [*de Leeuw et al.*, 2013], as well as for measuring volcanic ash plume proper-
334 ties [*Grainger et al.*, 2013; *Virtanen et al.*, 2014]. AATSR has the advantage of pro-
335 viding measurements at two viewing angles (near-nadir and 55° forward), as well as at
336 NIR and TIR wavebands, which facilitate the discrimination between volcanic ash and
337 water or ice clouds. Importantly, the AATSR, similar to most other satellite instruments,
338 measures only the intensity of radiation (of which the angle distribution is described by
339 $P_{11}(\theta)$) [*Tanré et al.*, 2011]. Some satellite based instruments, however, e.g. POLDER
340 (POLarization and Directionality of the Earth’s Reflectances) aboard PARASOL, can
341 also measure the linear polarization of the radiation (P_{12}/P_{11}) [*Deschamps et al.*, 1994].
342 POLDER has recently also been used to investigate airborne volcanic ash from Eyjafjal-
343 lajökull [*Waquet et al.*, 2014].

344 Depending on the across track position, the viewing angle of AATSR varies between 0°
345 and 22° for the near-nadir view, and between 52° and 56° for the forward view. Taking
346 into account the Sun-satellite geometry, the scattering angle for AATSR measurements
347 varies mostly between 50° and 170° . We will thus consider how our results are affected,
348 when we account for the fact that AATSR measurements do not cover the whole angular
349 span from exact backscattering to forward scattering.

350 Multiple scattering becomes substantial with large aerosol optical depths, in which case
351 the signal measured by the AATSR will be affected significantly also by polarization
352 components and all scattering angles are relevant. It has been shown, for example, that
353 neglect of polarization may then lead to considerable errors [*Moreno et al.*, 2002; *D. M.*
354 *Stam and J. W. Hovenier*, 2005]. It can thus be expected that the ellipsoids may provide
355 substantial improvements on simpler model particles (spheres or spheroids [*Dubovik et al.*,

2006; Yang et al., 2007]) as their performance in reproducing the whole scattering matrix is better [Bi et al., 2009]. Thus, for this case, the investigation carried out in the previous section is appropriate, but the assessment of the performance requires full radiative transfer simulations and is outside the scope of the present study. We will consider these and full retrieval tests in a follow-up study.

When the aerosol optical depth is low, however, which is usually the situation [Remer et al., 2008; Colarco et al., 2014], single scattering dominates the aerosol signal measured by AATSR. For testing the performance of ellipsoids in this situation, only considering the phase function is required. The approach is then, as a sensitivity test, to repeat the treatment of Sect. 3, but only considering the relevant angular range and scattering-matrix elements. However, for curiosity, we will also consider fitting simultaneously both P_{11} and P_{12}/P_{11} matrix elements, as this would be relevant for the POLDER instrument.

The best-fit shape distributions for the AATSR case, when fitting only the phase function P_{11} or both phase function and depolarization P_{12}/P_{11} simultaneously, are shown in Figures 8 and 9 respectively. The fits themselves (not shown) were, as can be expected, better than in the cases where the whole matrix element was fitted simultaneously (Figures 5 and 6). Improvement over the spheres was evident. Here again, as previously for the whole matrix in Figure 7, we can see the tendency of best-fits to avoid pure prolate shapes. Also, the phase function fit especially seems to have only moderately asymmetric shapes involved with axis ratios smaller than 2.5. Fits for the different wavelengths appear similar, which is encouraging. Also, as expected, when we only focus on a certain angle range, the fitting improves in that angle range but loses precision at other angles. The same inevitably happens when the fitting is concentrated on just some matrix elements

379 and the others are omitted, i.e. the fits for the other matrix elements considerably worsen,
380 while those that are considered are fitted quite well.

4.3. Suggested Generic Shape Distribution

381 The good performance, and the similarity of the best-fit distributions to those obtained
382 in Sect. 4.2 suggest that ellipsoids will improve the performance of the AATSR retrieval.
383 An equiprobable shape distribution, although omitting some of the special features of the
384 best-fit distributions, provides an adequately working first guess alternative for the best-fit
385 shape distribution. Moreover, for the AATSR satellite measurements point of view, as can
386 be deduced from Figure 8, a more refined and yet symmetric shape distribution could be
387 formed by an equiprobable distribution from which all the model particles with axis ratios
388 larger than 2.5 would be discarded. Even further refinement could be achieved by omitting
389 pure prolate shapes. This kind of more refined shape distribution and an equiprobable
390 distribution are compared for Eyjafjallajökull in Figure 10, where the whole scattering
391 matrix is shown when the fits are performed only for the P_{11} element. It can be seen how
392 the best-fit shape distribution (solid black line) follows the measurements (red marks)
393 for the P_{11} element quite well, but performs equally badly, as is expected, or even worse
394 for the other elements than the equiprobable distribution (green line). The suggested
395 refined shape distribution (shown in dashed black line) does not markedly improve on
396 the equiprobable distribution in modeling the phase function and performs visibly worse
397 on fitting the measurements for elements P_{22}/P_{11} and P_{34}/P_{11} . The performance of the
398 refined shape distribution for the other samples was similar to that from Eyjafjallajökull,
399 thus it can be concluded that the more refined shape distribution considered here is not

400 worth the added effort and simpler equiprobable distribution is the most reasonable first-
401 guess distribution that can always be expected to improve significantly on Mie models.

5. Summary and Conclusions

402 We present new measurements of the scattering matrices as functions of the scatter-
403 ing angle of two volcanic ash samples corresponding to the Eyjafjallajökull and Puyehue
404 volcanic eruptions. The samples were collected after the April 2010 and June 2011 erup-
405 tions, respectively. Measurements are performed at 647 nm covering the scattering angle
406 range from 3° to 177° . To facilitate the use of the experimental scattering matrices for
407 multiple-scattering calculations, we have obtained synthetic scattering matrices based on
408 the measurements in the full scattering angle range from 0° to 180° . Tables of the mea-
409 sured and synthetic scattering matrices are available in the Amsterdam-Granada Light
410 Scattering Database: www.iaa.es/scattering. The data are freely available under request
411 or citation of this paper and [Muñoz *et al.*, 2012].

412 We have used ellipsoidal shapes in an effort to produce scattering matrix elements
413 measured from samples collected near various volcanic sources. This was done in order to
414 assess whether ellipsoidal model particles could be used to model single scattering of light
415 by volcanic ash particles. Note that the retrieved shape distributions do not necessarily
416 reflect the real sample particle shape distributions. For example, it has been shown in case
417 of spheroids that the best-fit shape distribution of model shapes do not clearly correlate
418 with the target shape distribution [Nousiainen *et al.*, 2011].

419 The best-fitting shape distributions of ellipsoidal model particles were sought and their
420 fits to the measurements assessed both for the whole scattering matrix and for the point
421 of view of the AATSR instrument (only phase function at a certain angle span), as well

422 as for the point of view of satellite instruments able to also measure the polarization
423 (combination of phase function and linear polarization element of the scattering matrix,
424 P_{12}/P_{11}) separately. The results could be used for example to improve data interpretation
425 from remote sensing satellites such as AATSR.

426 Ellipsoids prove to be rather good shapes for modeling the optical properties of volcanic
427 ash for all the samples and at all the wavelengths tested here. Although considerably
428 improving over spherical model particles, they nevertheless have also shortcomings. The
429 depolarization P_{22}/P_{11} turns out to be especially hard to fit adequately. The results imply
430 that ellipsoids, conveniently available in a well-organized database by *Meng et al.* [2010],
431 provide an adequately working set of model shapes for forward modeling applications. For
432 inverse problems their use may be more problematic. For example, it was shown by *Kemp-*
433 *pinen et al.* [2015] that ellipsoids do not seem to be suitable for retrievals of refractive index
434 and the same probably holds true for retrievals of other physical characteristics as well.
435 This might also explain why we obtained better results when using the higher refractive
436 index, representative of the bulk matter ($m = 1.55 + 0.001i$), than with the assumed
437 smaller indices of the more porous particles, although these smaller indices would have
438 been closer to the estimated refractive indices of the ash samples (Table 1). Regardless
439 of these issues, however, the ellipsoids are the best currently available model particle for
440 real applications due to their considerable parameter space to consider. In particular, the
441 required range of size parameters involved is substantial, demanding further development
442 and ever improving computing power for more sophisticated modelling approaches.

443 Finally, on forward modeling the equiprobable shape distribution of ellipsoids was found
444 to be a very good compromise between simplicity and performance. A more refined

445 generalized shape distribution was also tested and discussed, but the advantage it provided
446 over more general equiprobable distribution was small at best. The equiprobable shape
447 distribution is thus recommended as a first-guess shape distribution on applications where
448 the shape distributions cannot be optimized for the purpose.

449 **Acknowledgments.**

450 We thank Zhaokai Meng for letting us use his ellipsoid database, without which this
451 study would not have materialized in its current form. It is a pleasure also to thank
452 Evgenia Ilinskaya and Alberto Caselli for providing the Eyjafjallajökull and Puyehue
453 samples, respectively. The SEM pictures were taken at the Scientific Instrumentation
454 Center of the University of Granada. We are indebted to Isabel Guerra-Tschuschke for
455 her support with the SEM.

456 This work has been supported by the Plan Nacional de Astronomía y Astrofísica (con-
457 tracts AYA2009-08190 and AYA2012-39691), Junta de Andalucía (contract P09-FMQ-
458 455), VAST project by ESA (ESA-ESRIN contract 4000105701/12/I-LG), Finnish Fund-
459 ing Agency for Technology and Innovation (Tekes) (grant 3155/31/2009), Academy of
460 Finland (grant 255718), Academy of Finland Centre on Excellence in Atmospheric Sci-
461 ence (project 272041) and the Top-level Research Initiative (TRI) CRAICC (Cryosphere-
462 atmosphere interactions in a changing Arctic climate).

463 Volcanic ash particle measurements presented in this paper are freely available at the
464 Amsterdam-Granada Light Scattering Database (www.iaa.es/scattering; *Muñoz et al.*
465 [2012]). Alternatively, data can be requested from Olga Muñoz (olga@iaa.es).

References

- 466 Baum, B. A., P. Yang, Y.-X. Hu, and Q. Feng (2010), The impact of ice particle roughness
467 on the scattering phase matrix, *Journal of Quantitative Spectroscopy and Radiative*
468 *Transfer*, *111*(1718), 2534 – 2549, doi:10.1016/j.jqsrt.2010.07.008.
- 469 Baxter, P. J., R. S. Bernstein, H. Falk, J. French, and R. Ing (1982), Medical aspects
470 of volcanic disasters: An outline of the hazards and emergency response measures,
471 *Disasters*, *6*(4), 268–276, doi:10.1111/j.1467-7717.1982.tb00549.x.
- 472 Bertrand, C., J.-P. van Ypersele, and A. Berger (1999), Volcanic and solar impacts on
473 climate since 1700, *Climate Dynamics*, *15*(5), 355–367, doi:10.1007/s003820050287.
- 474 Bertrand, C., J.-P. van Ypersele, and A. Berger (2002), Are natural climate forcings able
475 to counteract the projected anthropogenic global warming?, *Climatic Change*, *55*(4),
476 413–427, doi:10.1023/A:1020736804608.
- 477 Bi, L., P. Yang, G. Kattawar, and R. Kahn (2009), Single-scattering properties of triaxial
478 ellipsoidal particles for a size parameter range from the rayleigh to geometric-optics
479 regimes, *Applied Optics*, *48*(1), doi:10.1016/j.jaerosci.2010.02.008.
- 480 Bignami, C., V. Bosi, L. Costantin, C. Cristiani, F. Lavigne, and P. Thierry (Eds.) (2013),
481 *Handbook for Volcanic Risk Management - Prevention, Crisis Management, Resilience,*
482 *MIAVITA.*
- 483 Casadevall, T. J. (1994), The 1989-1990 eruption of Redoubt volcano, Alaska: impacts
484 on aircraft operations, *Journal of Volcanology and Geothermal Research*, *62*(1–4), 301
485 – 316, doi:10.1016/0377-0273(94)90038-8.
- 486 Colarco, P. R., R. A. Kahn, L. A. Remer, and R. C. Levy (2014), Impact of satellite
487 viewing-swath width on global and regional aerosol optical thickness statistics and

488 trends, *Atmospheric Measurement Techniques*, 7(7), 2313–2335, doi:10.5194/amt-7-
489 2313-2014.

490 D. M. Stam, and J. W. Hovenier (2005), Errors in calculated planetary phase functions
491 and albedos due to neglecting polarization, *Astronomy & Astrophysics*, 444(1), 275–286,
492 doi:10.1051/0004-6361:20053698.

493 de Leeuw, G., T. Holzer-Popp, S. Bevan, W. H. Davies, J. Descloitres, R. G. Grainger,
494 J. Griesfeller, A. Heckel, S. Kinne, L. Klser, P. Kolmonen, P. Litvinov, D. Martynenko,
495 P. North, B. Ovigneur, N. Pascal, C. Poulsen, D. Ramon, M. Schulz, R. Siddans,
496 L. Sogacheva, D. Tanr, G. E. Thomas, T. H. Virtanen, W. von Hoyningen Huene,
497 M. Vountas, and S. Pinnock (2013), Evaluation of seven European aerosol optical
498 depth retrieval algorithms for climate analysis, *Remote Sensing of Environment*, doi:
499 10.1016/j.rse.2013.04.023.

500 Deschamps, P., F. M. Bréon, M. Leroy, A. Podaire, A. Bricaud, J. Buriez, and G. Seze
501 (1994), The POLDER mission: Instrument characteristics and scientific objectives,
502 *IEEE Trans. Geosc. Rem. Sens.*, 32, 598–615, doi:10.1109/36.297978.

503 Dubovik, O., A. Sinyuk, T. Lapyonok, B. N. Holben, M. Mishchenko, P. Yang, T. F.
504 Eck, H. Volten, O. Muoz, B. Veihelmann, W. J. van der Zande, J.-F. Leon, M. Sorokin,
505 and I. Slutsker (2006), Application of spheroid models to account for aerosol parti-
506 cle nonsphericity in remote sensing of desert dust, *Journal of Geophysical Research:*
507 *Atmospheres*, 111(D11), doi:10.1029/2005JD006619.

508 Grainger, R., D. Peters, G. Thomas, A. Smith, R. Siddans, E. Carboni, and A. Dubhia
509 (2013), Measuring volcanic plume and ash properties from space, *Geological Society,*
510 *London, Special Publications*, 380, doi:10.1144/SP380.7.

- 511 Gudmundsson, G. (2011), Respiratory health effects of volcanic ash with special reference
512 to Iceland. A review, *The Clinical Respiratory Journal*, 5(1), 2–9, doi:10.1111/j.1752-
513 699X.2010.00231.x.
- 514 Gudmundsson, M., G. Larsen, A. Höskuldsson, and A. Gylfason (2008), Volcanic hazards
515 in Iceland, *Jökull*, (58), 251 – 268.
- 516 Guffanti, M., D. J. Schneider, K. L. Wallace, T. Hall, D. R. Bensimon, and L. J. Salinas
517 (2010), Aviation response to a widely dispersed volcanic ash and gas cloud from the
518 August 2008 eruption of Kasatochi, Alaska, USA, *Journal of Geophysical Research:*
519 *Atmospheres*, 115(D2), doi:10.1029/2010JD013868.
- 520 Hansen, J. E., and L. D. Travis (1974), Light scattering in planetary atmospheres, *Space*
521 *Sci. Rev.*, 16, 527–610, doi:10.1007/BF00168069.
- 522 Heiken, G. (1974), *An Atlas of Volcanic Ash*, Smithsonian Institution Press.
- 523 Horwell, C., and P. Baxter (2006), The respiratory health hazards of volcanic ash: a review
524 for volcanic risk mitigation, *Bulletin of Volcanology*, 69(1), 1–24, doi:10.1007/s00445-
525 006-0052-y.
- 526 Hovenier, J. (2000), Measuring scattering matrices of small particles at optical wave-
527 lengths, in *Light Scattering by Nonspherical Particles*, edited by M. I. Mishchenko,
528 J. W. Hovenier, and L. D. Travis, chap. 6, pp. 147–172, Academic Press, San Diego.
- 529 Hovenier, J., and D. Guirado (2014), Zero slopes of the scattering function and scattering
530 matrix for strict forward and backward scattering by mirror symmetric collections of
531 randomly oriented particles, *Journal of Quantitative Spectroscopy and Radiative Trans-*
532 *fer*, 133(0), 596 – 602, doi:10.1016/j.jqsrt.2013.09.023.

- 533 Hovenier, J., H. C. van de Hulst, and C. V. M. van der Meer (1986), Conditions for the
534 elements of the scattering matrix, *Astron. Astrophys.*, *157*, 301–310.
- 535 Hyde, W. T., and T. J. Crowley (2000), Probability of future climatically
536 significant volcanic eruptions, *J. Climate*, *13*, 1445–1450, doi:10.1175/1520-
537 0442(2000)013<1445:LOFCSV>2.0.CO;2.
- 538 Kahn, R. A., and J. Limbacher (2012), Eyjafjallajökull volcano plume particle-type char-
539 acterization from space-based multi-angle imaging, *Atmospheric Chemistry and Physics*,
540 *12*(20), 9459–9477, doi:10.5194/acp-12-9459-2012.
- 541 Kahnert, M., T. Nousiainen, and H. Lindqvist (2014), Review: Model particles in atmo-
542 spheric optics, *Journal of Quantitative Spectroscopy & Radiative Transfer*, *146*, 41–58.
- 543 Kemppinen, O., T. Nousiainen, and S. Merikallio (2015), On retrieving dust particle
544 refractive index using shape distributions of ellipsoids, *J. Geophys. Res. Atmos.*, sub-
545 mitted.
- 546 Konert, M., and J. Vandenberghe (1997), Comparison of laser grain size analysis with
547 pipette and sieve analysis: a solution for the underestimation of the clay fraction,
548 *Sedimentology*, *44*(3), 523–535, doi:10.1046/j.1365-3091.1997.d01-38.x.
- 549 Kylling, A., M. Kahnert, H. Lindqvist, and T. Nousiainen (2014), Volcanic ash infrared
550 signature: porous non-spherical ash particle shapes compared to homogeneous spherical
551 ash particles, *Atmospheric Measurement Techniques*, *7*(4), 919–929, doi:10.5194/amt-
552 7-919-2014.
- 553 Llewellyn-Jones, D., M. C. Edwards, C. T. Mutlow, A. R. Birks, I. J. Barton, and H. Tait
554 (2001), AATSR: global-change and surface-temperature measurements from Envisat,
555 *ESA Bulletin*, *105*, 11–21.

- 556 Mackie, S., S. Millington, and I. M. Watson (2014), How assumed composition affects
557 the interpretation of satellite observations of volcanic ash, *Meteorological Applications*,
558 *21*(1), 20–29, doi:10.1002/met.1445.
- 559 Maria, A., and S. Carey (2002), Using fractal analysis to quantitatively characterize the
560 shapes of volcanic particles, *Journal of Geophysical Research: Solid Earth*, *107*(B11),
561 ECV 7–1–ECV 7–17, doi:10.1029/2001JB000822.
- 562 Mather, T., D. Pyle, and C. Oppenheimer (2013), *Tropospheric Volcanic Aerosol*, pp.
563 189–212, American Geophysical Union, doi:10.1029/139GM12.
- 564 McGee, T. J., P. Newman, M. Gross, U. Singh, S. Godin, A.-M. Lacoste, and G. Megie
565 (1994), Correlation of ozone loss with the presence of volcanic aerosols, *Geophysical*
566 *Research Letters*, *21*(25), 2801–2804, doi:10.1029/94GL02350.
- 567 Meng, Z., P. Yang, G. Kattawar, L. Bi, K. Liou, and I. Laszlo (2010), Single-scattering
568 properties of tri-axial ellipsoidal mineral dust aerosols: A database for applica-
569 tion to radiative transfer calculations, *Journal of Aerosol Science*, *41*, 501–512, doi:
570 10.1016/j.jaerosci.2010.02.008.
- 571 Merikallio, S., H. Lindqvist, T. Nousiainen, and M. Kahnert (2011), Modelling light scat-
572 tering by mineral dust using spheroids: assessment of applicability, *Atmospheric Chem-*
573 *istry and Physics*, *11*(11), 5347–5363, doi:10.5194/acp-11-5347-2011.
- 574 Merikallio, S., T. Nousiainen, M. Kahnert, and A.-M. Harri (2013), s, *Optics Express*, *21*,
575 17,972–17,985, doi:10.1364/OE.21.017972.
- 576 Mishchenko, M. I., J. W. Hovenier, and L. D. Travis (Eds.) (2000), *Light Scattering by*
577 *Nonspherical Particles*, Academic Press, San Diego, 690 pp.

- 578 Moreno, F., O. Muoz, J. Lpez-Moreno, A. Molina, and J. Ortiz (2002), A monte carlo
579 code to compute energy fluxes in cometary nuclei, *Icarus*, *156*(2), 474 – 484, doi:
580 <http://dx.doi.org/10.1006/icar.2001.6806>.
- 581 Muñoz, O., H. Volten, J. W. Hovenier, B. Veihelmann, W. J. van der Zande, L. B.
582 F. M. Waters, and W. I. Rose (2004), Scattering matrices of volcanic ash particles
583 of Mount St. Helens, Redoubt, and Mount Spurr volcanoes, *J. Geophys. Res.*, *109*,
584 doi:10.1029/2004JD004684.
- 585 Muñoz, O., H. Volten, J. W. Hovenier, T. Nousiainen, K. Muinonen, D. Guirado,
586 F. Moreno, and L. B. F. M. Waters (2007), Scattering matrix of large Saharan dust par-
587 ticles: Experiments and computations, *Journal of Geophysical Research: Atmospheres*,
588 *112*(D13), doi:10.1029/2006JD008074.
- 589 Muñoz, O., F. Moreno, D. Guirado, J. Ramos, A. Lpez, F. Girela, J. Jernimo, L. Cos-
590 tillo, and I. Bustamante (2010), Experimental determination of scattering matrices
591 of dust particles at visible wavelengths: The IAA light scattering apparatus, *Jour-
592 nal of Quantitative Spectroscopy and Radiative Transfer*, *111*(1), 187 – 196, doi:
593 [10.1016/j.jqsrt.2009.06.011](http://dx.doi.org/10.1016/j.jqsrt.2009.06.011).
- 594 Muñoz, O., F. Moreno, D. Guirado, J. Ramos, H. Volten, and J. Hovenier (2011), The
595 IAA cosmic dust laboratory: Experimental scattering matrices of clay particles, *Icarus*,
596 *211*(1), 894 – 900, doi:10.1016/j.icarus.2010.10.027.
- 597 Muñoz, O., F. Moreno, D. Guirado, D. Dabrowska, H. Volten, and J. Hovenier (2012), The
598 Amsterdam – Granada light scattering database, *Journal of Quantitative Spectroscopy
599 and Radiative Transfer*, *113*(7), 565 – 574, doi:10.1016/j.jqsrt.2012.01.014.

- 600 Newman, S. M., L. Clarisse, D. Hurtmans, F. Marengo, B. Johnson, K. Turnbull, S. Have-
601 mann, A. J. Baran, D. O’Sullivan, and J. Haywood (2012), A case study of observa-
602 tions of volcanic ash from the Eyjafjallajökull eruption: 2. airborne and satellite ra-
603 diative measurements, *Journal of Geophysical Research: Atmospheres*, *117*(D20), doi:
604 10.1029/2011JD016780.
- 605 Nousiainen, T., and K. Muinonen (2007), Surface-roughness effects on single-scattering
606 properties of wavelength-scale particles, *J. Quant. Spectrosc. Radiat. Transfer*, *106*,
607 389–397, doi:10.1016/j.jqsrt.2007.01.024.
- 608 Nousiainen, T., M. Kahnert, and H. Lindqvist (2011), Can particle shape information
609 be retrieved from light-scattering observations using spheroidal model particles?, *Jour-
610 nal of Quantitative Spectroscopy and Radiative Transfer*, *112*(13), 2213 – 2225, doi:
611 10.1016/j.jqsrt.2011.05.008.
- 612 Pollack, J., O. Toon, and B. Khare (1974), Optical properties of some terrestrial rocks
613 and glasses, *Icarus*, *19*, 372–389, doi:10.1016/0019-1035(73)90115-2.
- 614 Prata, A. J., C. Zehner, and K. Stebel (2014), Earth observations and volcanic ash, *A
615 report of the ESA/Eumosat Workshop, 47 March, 2013*, doi:10.5270/atmva-14-04.
- 616 Remer, L. A., R. G. Kleidman, R. C. Levy, Y. J. Kaufman, D. Tanr, S. Mattoo, J. V.
617 Martins, C. Ichoku, I. Koren, H. Yu, and B. N. Holben (2008), Global aerosol clima-
618 tology from the modis satellite sensors, *Journal of Geophysical Research: Atmospheres*,
619 *113*(D14), n/a–n/a, doi:10.1029/2007JD009661.
- 620 Riley, C. M., W. I. Rose, and G. J. S. Bluth (2003), Quantitative shape measurements
621 of distal volcanic ash, *Journal of Geophysical Research: Solid Earth*, *108*(B10), doi:
622 10.1029/2001JB000818.

- 623 Rocha-Lima, A., J. V. Martins, L. A. Remer, N. A. Krotkov, M. H. Tabacniks, Y. Ben-
624 Ami, and P. Artaxo (2014), Optical, microphysical and compositional properties of the
625 Eyjafjallajökull volcanic ash, *Atmospheric Chemistry and Physics Discussions*, *14*(9),
626 13,271–13,300, doi:10.5194/acpd-14-13271-2014.
- 627 Schumann, U., B. Weinzierl, O. Reitebuch, H. Schlager, A. Minikin, C. Forster, R. Bau-
628 mann, T. Sailer, K. Graf, H. Mannstein, C. Voigt, S. Rahm, R. Simmet, M. Scheibe,
629 M. Lichtenstern, P. Stock, H. Rüba, D. Schäuble, A. Tafferner, M. Rautenhaus, T. Gerz,
630 H. Ziereis, M. Krautstrunk, C. Mallaun, J.-F. Gayet, K. Lieke, K. Kandler, M. Ebert,
631 S. Weinbruch, A. Stohl, J. Gasteiger, S. Groß, V. Freudenthaler, M. Wiegner, A. Ans-
632 mann, M. Tesche, H. Olafsson, and K. Sturm (2011), Airborne observations of the Ey-
633 jafjalla volcano ash cloud over Europe during air space closure in April and May 2010,
634 *Atmospheric Chemistry and Physics*, *11*(5), 2245–2279, doi:10.5194/acp-11-2245-2011.
- 635 Sparks, R. (2003), Forecasting volcanic eruptions, *Earth and Planetary Science Letters*,
636 *210*(12), 1 – 15, doi:10.1016/S0012-821X(03)00124-9.
- 637 Stevenson, J. A., S. C. Millington, F. M. Beckett, G. T. Swindles, and T. Thordarson
638 (2015), Big grains go far: reconciling tephrochronology with atmospheric measurements
639 of volcanic ash, *Atmospheric Measurement Techniques Discussions*, *8*(1), 65–120, doi:
640 10.5194/amtd-8-65-2015.
- 641 Tanré, D., F. M. Bréon, J. L. Deuzé, O. Dubovik, F. Ducos, P. François, P. Goloub,
642 M. Herman, A. Lifermann, and F. Waquet (2011), Remote sensing of aerosols by using
643 polarized, directional and spectral measurements within the A-train: the PARASOL
644 mission, *Atmospheric Measurement Techniques*, *4*(7), 1383–1395, doi:10.5194/amt-4-
645 1383-2011.

- 646 Virtanen, T. H., P. Kolmonen, E. Rodríguez, L. Sogacheva, A.-M. Sundström, and
647 G. de Leeuw (2014), Ash plume top height estimation using AATSR, *Atmospheric*
648 *Measurement Techniques*, 7(8), 2437–2456, doi:10.5194/amt-7-2437-2014.
- 649 Volten, H., O. Muñoz, J. F. de Haan, W. Vassen, J. W. Hovenier, K. Muinonen, and
650 T. Nousiainen (2001), Scattering matrices of mineral aerosol particles at 441.6 nm and
651 632.8 nm, *J. Geophys. Res.*, 106(D15), 17,375–17,401, doi:10.1029/2001JD900068.
- 652 Waquet, F., F. Peers, P. Goloub, F. Ducos, F. Thieuleux, Y. Derimian, J. Riedi, M. Chami,
653 and D. Tanré (2014), Retrieval of the Eyjafjallajökull volcanic aerosol optical and micro-
654 physical properties from POLDER/PARASOL measurements, *Atmospheric Chemistry*
655 *and Physics*, 14(4), 1755–1768, doi:10.5194/acp-14-1755-2014.
- 656 Yang, P., Q. Feng, G. Hong, G. W. Kattawar, W. J. Wiscombe, M. I. Mishchenko,
657 O. Dubovik, I. Laszlo, and I. N. Sokolik (2007), Modeling of the scattering and radiative
658 properties of nonspherical dust-like aerosols, *Journal of Aerosol Science*, 38(10), 995 –
659 1014, doi:http://dx.doi.org/10.1016/j.jaerosci.2007.07.001.

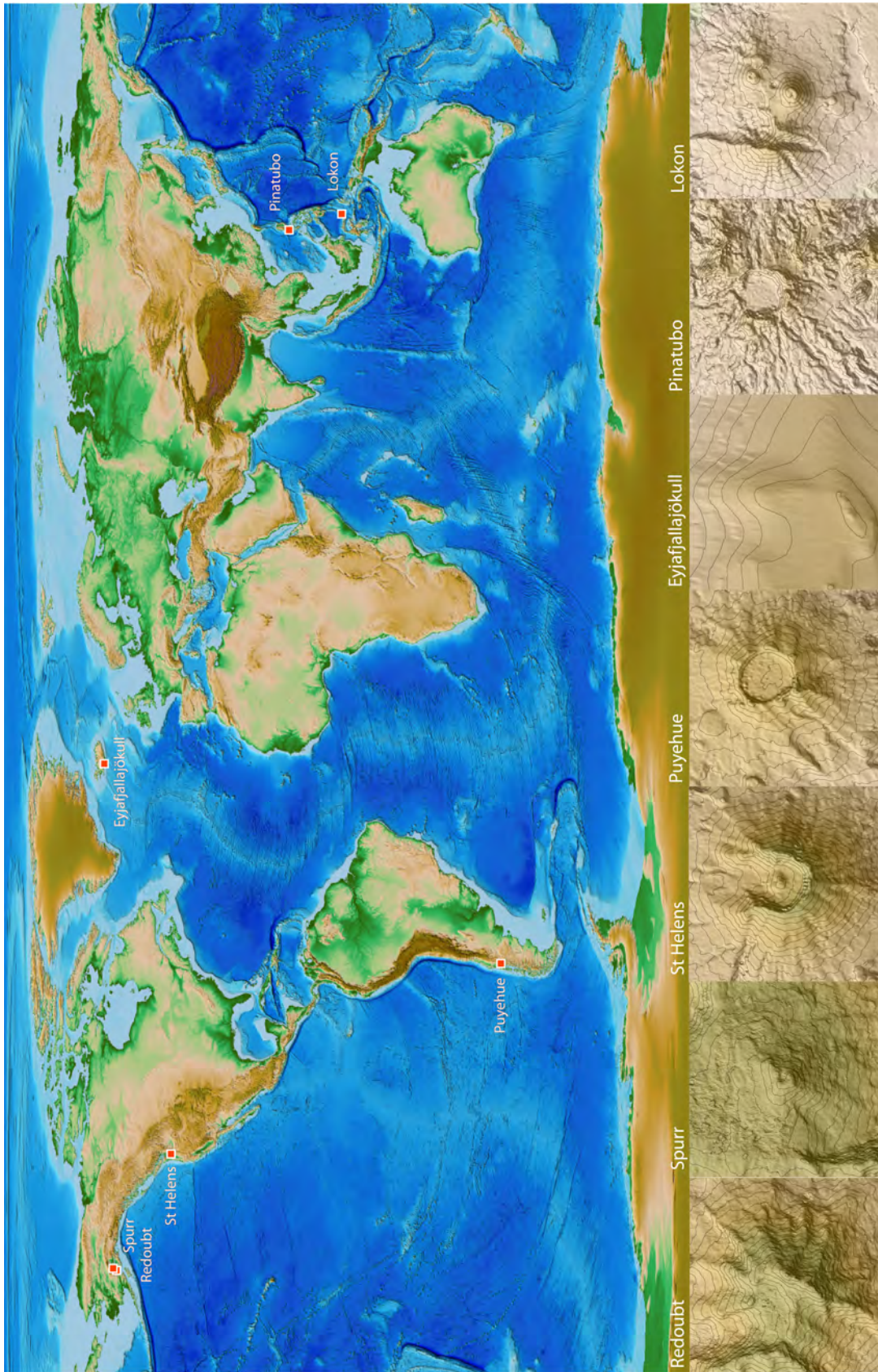


Figure 1. Map showing the locations of the volcanoes used here for model validation. Also shown are close-ups of each volcano within a 10 x 10 km box showing the height contours with 100 meters of vertical difference between the lines.

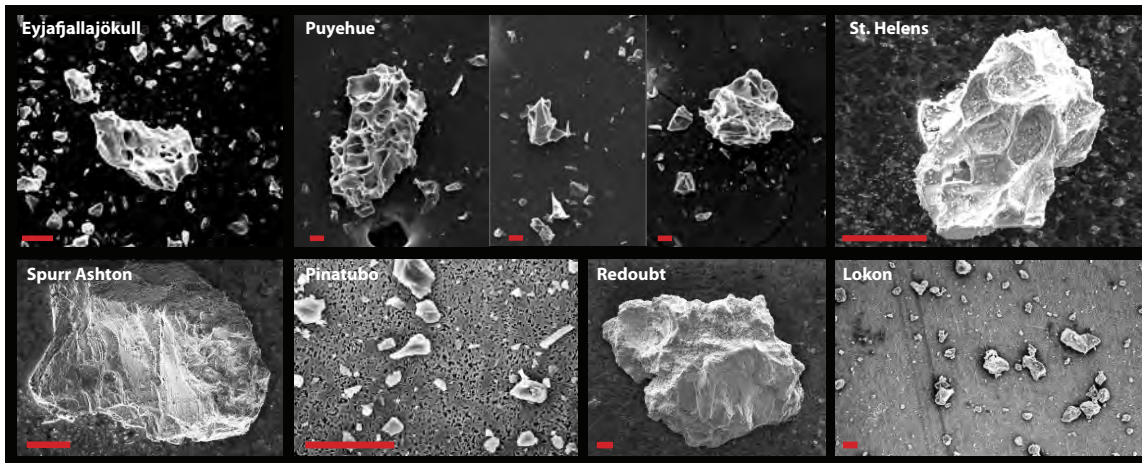


Figure 2. Collage of SEM-pictures for each of the volcanic ash samples discussed in this paper. The red bars equal 20 μm in all cases.

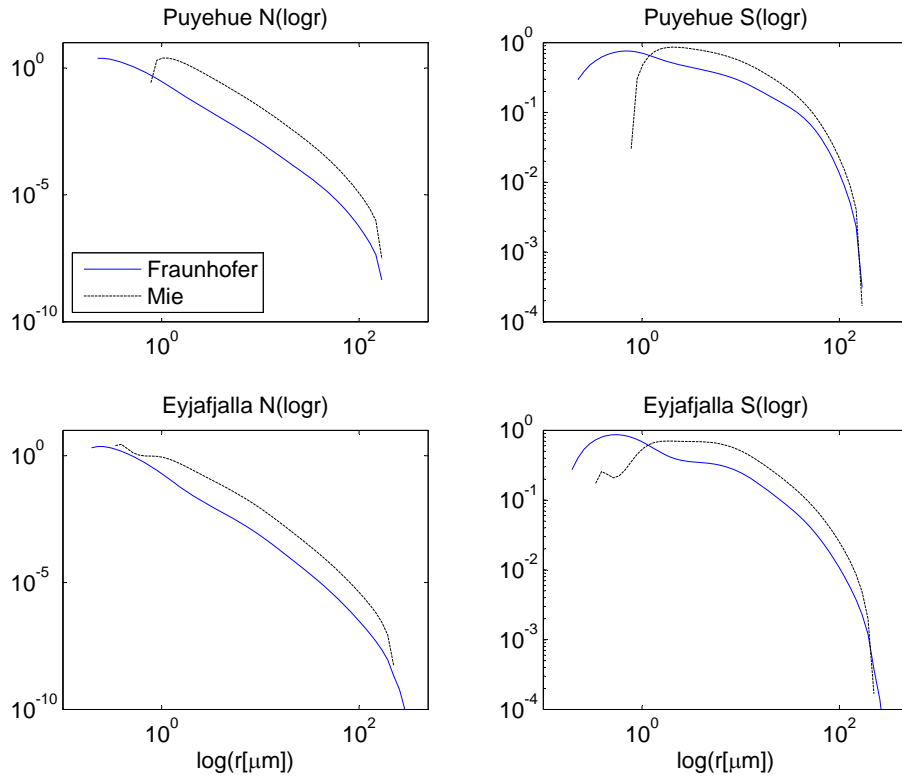


Figure 3. Measured size distributions $S(\log r)$ and $N(\log r)$, for projected surface area and particle number, respectively, retrieved from Puyehue and Eyjafjallajökull samples by using both Fraunhofer and Mie theories.

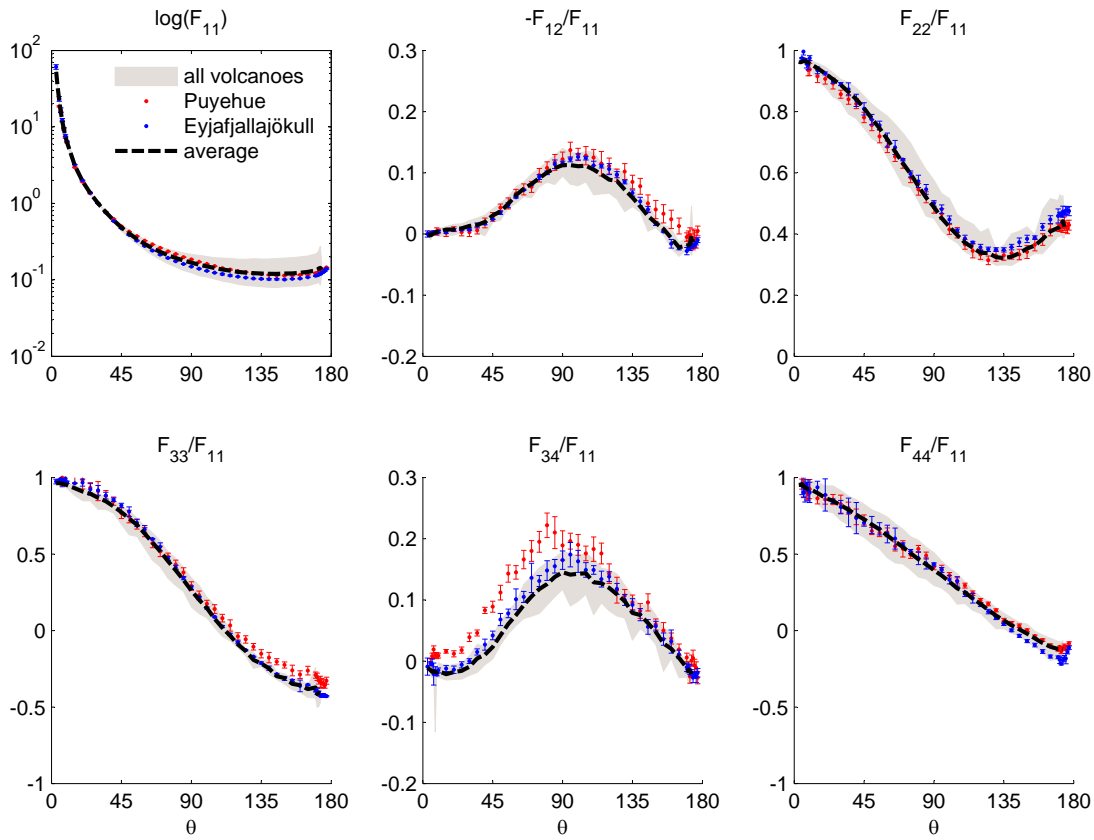


Figure 4. Measured scattering matrices for Puyehue (red) and Eyjafjallajökull (blue) samples for each of the scattering matrix elements. The average scattering matrix of all the volcanic ash particles in the Amsterdam–Granada database and the domain of the span of these particles are also shown.

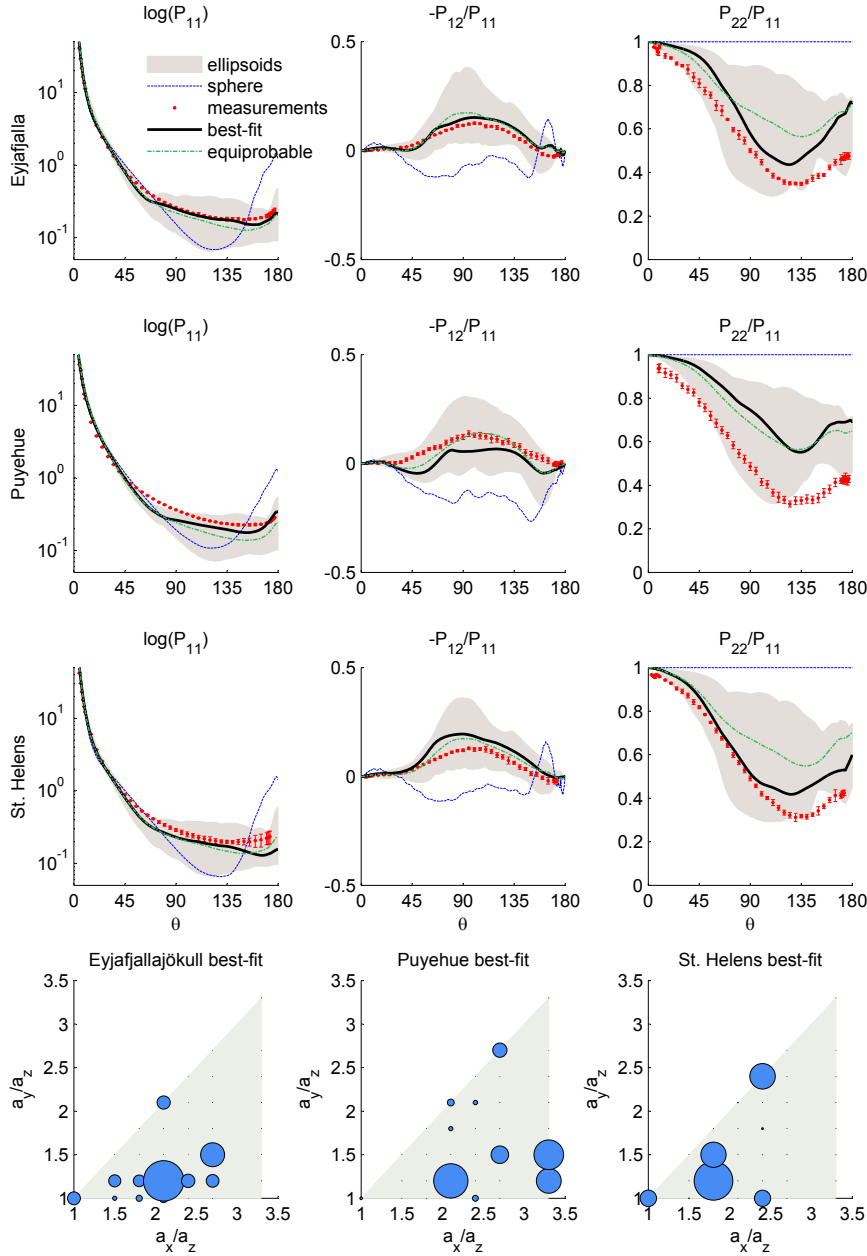


Figure 5. Best-fit ellipsoid model results and shape distributions (blue balls) for volcanic ash from Eyjafjallajökull, Puyehue and Helens (top to bottom, and from left to right in the last row of plots). Best-fit model results are shown for matrix elements P_{11} (shown on a logarithmic scale), P_{12}/P_{11} and P_{22}/P_{11} . The bottom row of plots shows the best-fit shape distributions for each of these ash types: along the axis are plotted the relative aspect ratios of the two biggest axes of the ellipsoid model particles, when the smallest axis is of unity length. The marker sizes are corresponding to the relative weights of corresponding shapes and the gray shading indicates the area covered by ellipsoids (sphere is excluded).

D R A F T

March 21, 2015, 9:14am

D R A F T

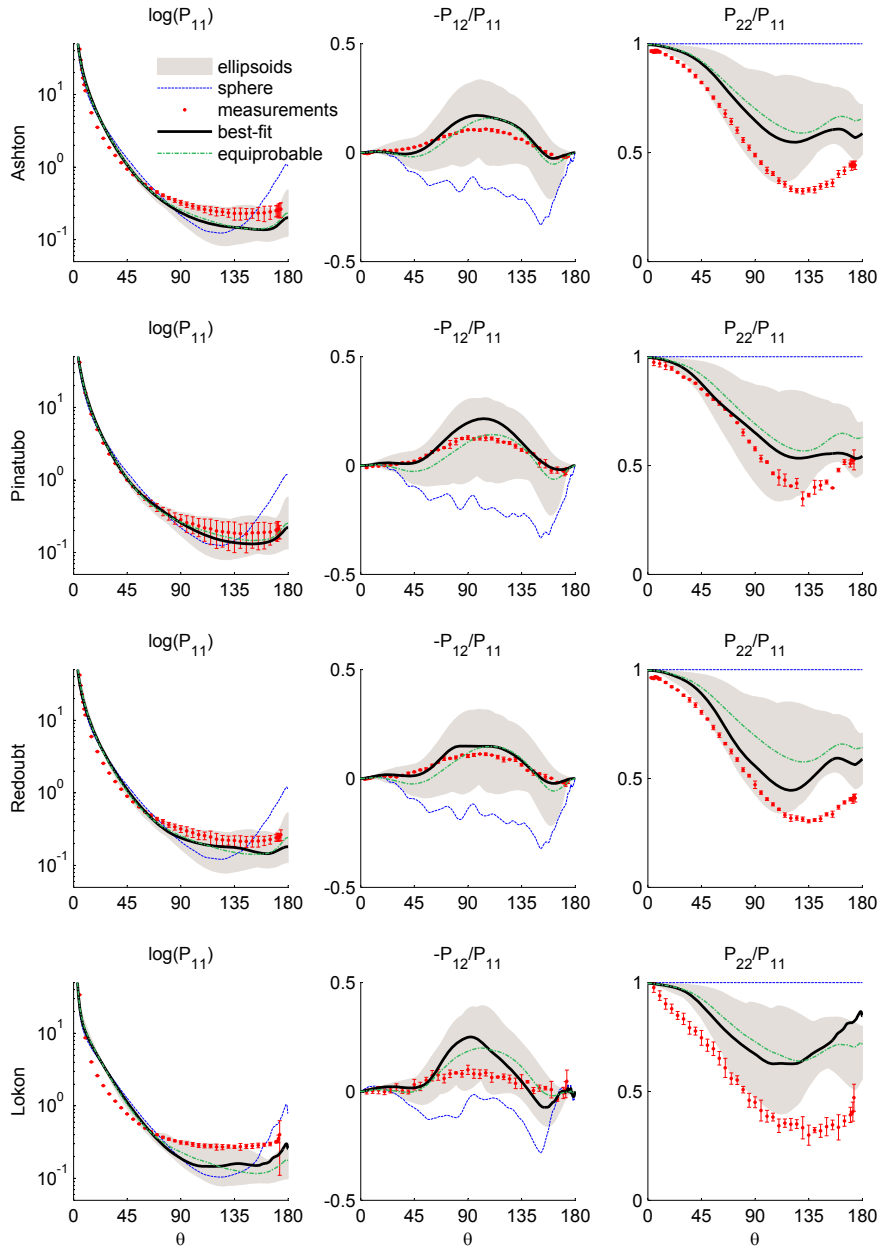


Figure 6. First three scattering matrix elements (columns) and best-fit ellipsoid models for four volcanic ash samples (rows): the best-fit model results for matrix elements P_{11} (shown on a logarithmic scale), P_{12}/P_{11} and P_{22}/P_{11} for the Ashton, Pinatubo, Redoubt, and Lokon volcanic ashes are shown.

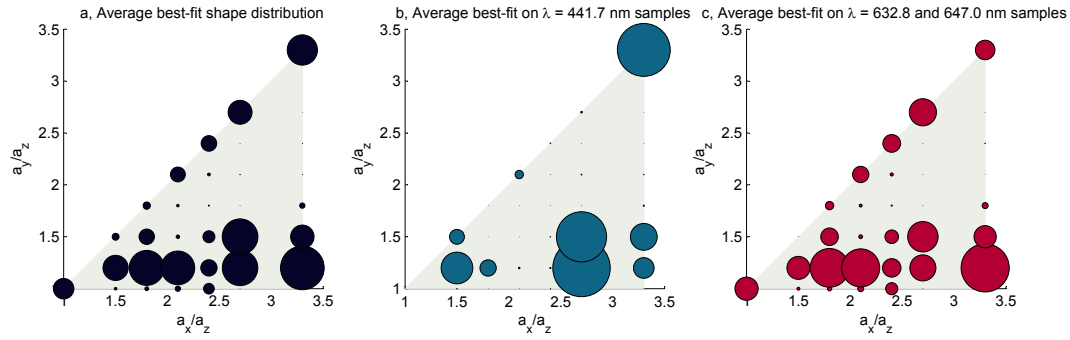


Figure 7. Best-fit shape distributions shown averaged over all samples and wavelengths (left subplot), for the shorter wavelength (center plot), and for the longer wavelength (right). Axes on the graph denote the major axis ratios of the model particles. The shaded area on the background denotes the region which the model ellipsoids considered in this study span.

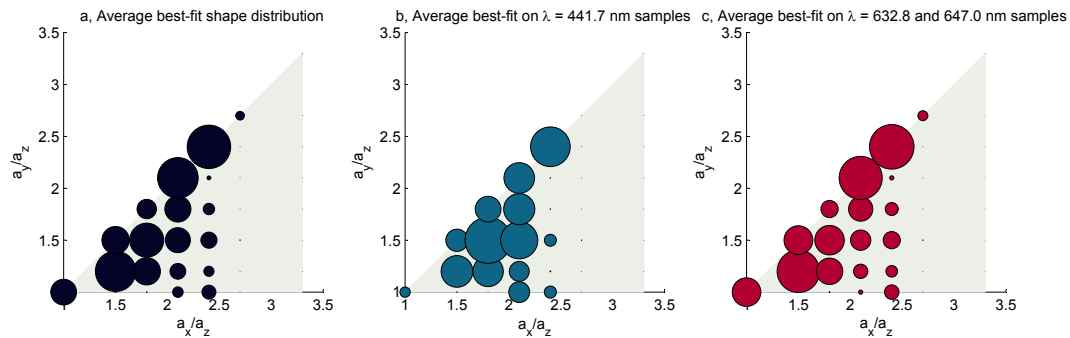


Figure 8. Best-fit shape distributions, when only the P_{11} element of the scattering matrix is fitted and only for the AATSR angle span. Labeling on this figure is the same as in Figure 7.

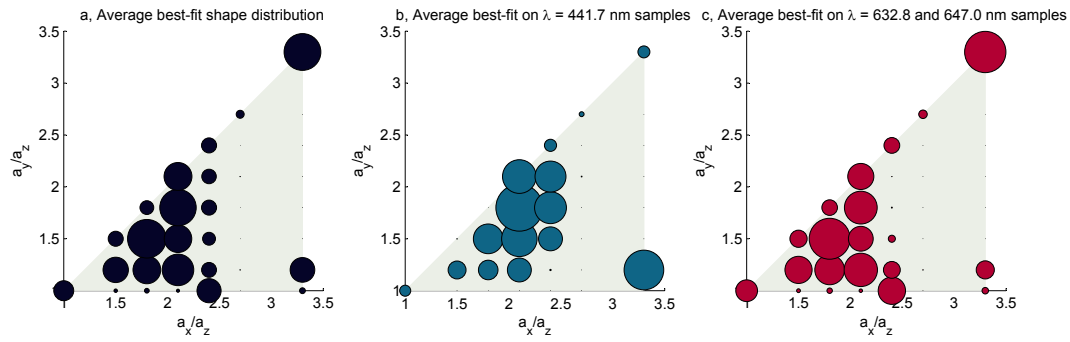
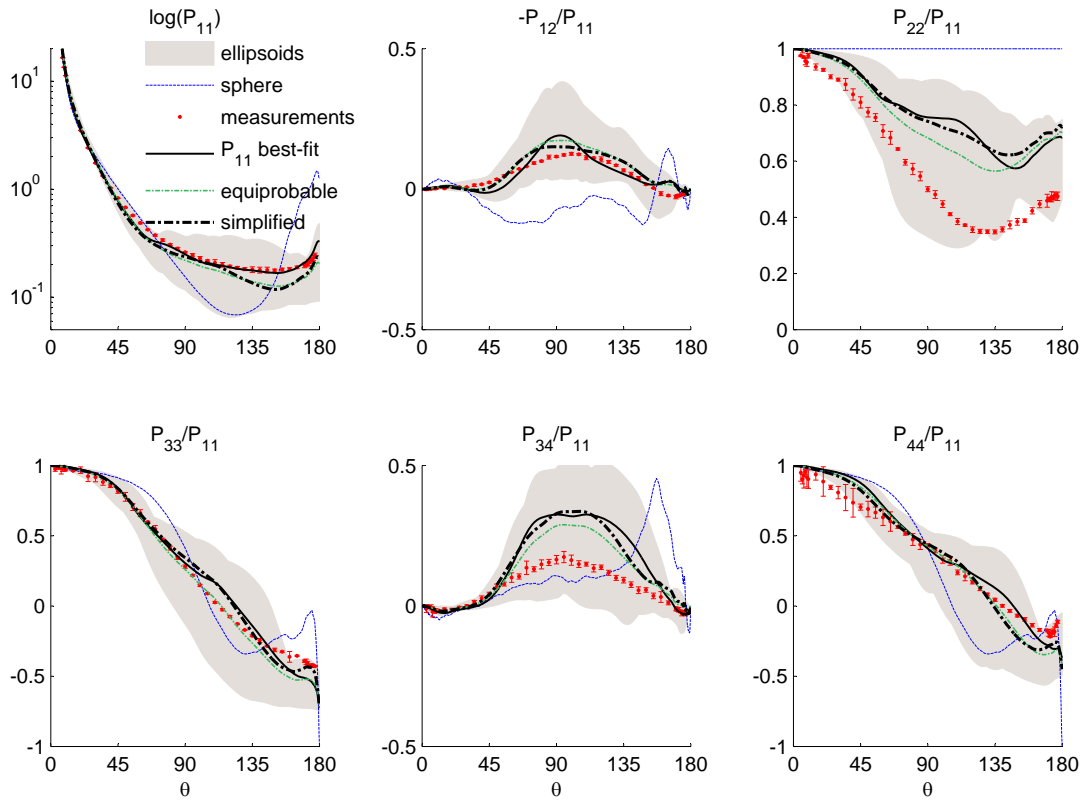


Figure 9. Best-fit shape distributions, when both P_{11} and P_{12} elements of the scattering matrix are fitted and only for the AATSR angle span. Labeling on this figure is the same as in Figure 7.

Table 1. Properties of measured Volcanic ash particles.

Sample	Mie		Fraunhofer		Refractive index		wavelength
	r_{eff} [μm]	ν_{eff}	r_{eff} [μm]	ν_{eff}	m_r, m_i (estimated)	λ [nm]	
Eyjafjallajökull	7.8	2.9	4.0	5.9	[1.43 – 1.59] + i[0 – 0.004]	647.0	
Lokon			7.0	2.5	[1.5 – 1.6] + i[0.001 – 0.00001]	441.6 & 632.8	
Pinatubo	8.0	5.1	2.9	12.4	[1.5 – 1.6] + i[0.001 – 0.00001]	441.6 & 632.8	
Puyehue	8.6	2.2	5.0	4.4	1.48 + i0.00027	647.0	
Redoubt A			4.1	9.7	[1.48 – 1.56] + i0.0018	632.8	
Spurr Ashton	5.2	3.4	2.6	4.9	[1.48 – 1.56] + i[0.0018 – 0.02]	632.8	
St. Helens	8.9	4.0	4.1	9.5	[1.48 – 1.56] + i0.0018	632.8	

**Figure 10.** Whole scattering matrix of Eyjafjallajökull: measurements and models with different shape distributions are shown. The best-fit model is fitted solely for P_{11} .